fluids

MDPI

*Article*

# Parametric Study of Unsteady Flow and Heat Transfer of Compressible Helium–Xenon Binary Gas through a Porous Channel Subjected to a Magnetic Field

**Pornthep Pattanavanitkul and Watit Pakdee ***

Center for R&D on Energy Efficiency in Thermo-Fluid Systems, Department of Mechanical Engineering, Faculty of Engineering, Thammasat School of Engineering, Thammasat University, Pathumthani 12121, Thailand; silentblaze-a@windowslive.com

* Correspondence: pwatit@engr.tu.ac.th

**Abstract:** A numerical analysis of unsteady fluid and heat transport of compressible Helium–Xenon binary gas through a rectangular porous channel subjected to a transverse magnetic field is herein presented. The binary gas mixture consists of Helium (He) and Xenon (Xe). In addition, the compressible gas properties are temperature-dependent. The set of governing equations are nondimensionalized via appropriate dimensionless parameters. The dimensionless equations involve a number of dimensionless groups employed for detailed parametric study. Consequently, the set of equations is discretized using a compact finite difference scheme and solved by using the 3rd-order Runge–Kutta method. The model's computed results are compared with data from past literature, and very favorable agreement is achieved. The results show that the magnetic field, compressibility and variable fluid properties profoundly affect heat and fluid transport. Variations of density with temperature as well as pressure result in an asymmetric mass flow profile. Furthermore, the friction coefficient is greater for the upper wall than for the lower wall due to larger velocity gradients along the top wall.

**Keywords:** magnetic field; compressible flow; binary gas; helium-xenon; porous channel



**Citation:** Pattanavanitkul, P.; Pakdee, W. Parametric Study of Unsteady Flow and Heat Transfer of Compressible Helium–Xenon Binary Gas through a Porous Channel Subjected to a Magnetic Field. *Fluids* **2021**, *6*, 392. https://doi.org/10.3390/fluids6110392

Academic Editor: Mahmoud Mamou

Received: 11 August 2021
Accepted: 22 October 2021
Published: 1 November 2021



## 1. Introduction

Magnetrohydrodynamics, known as MHD, is the combined field of fluid dynamics and electromagnetic effects. Theoretically, when electrically conducting fluids (such as noble gases and plasmas) flow through a magnetic field, electrons in both the fluid and the magnetic field induce an electric current in the direction perpendicular to the flow and magnetic field. The electric current then interacts with the magnetic field, which results in the "Lorentz force" being exerted on the fluid particles. In addition to the induced force, magnetic induction causes resistive heat, termed Joule or Ohmic heating. Magnetic fields can be utilized for a purpose of controlling flows, which are termed MHD flows. MHD applications include use as thrusters, pumps, accelerators and cross-field generators [1–4]. These MHD devices play a major role, for example, in enhancing the efficiency of jet engines [2]. In another example, plasma can be detained within the torus shape of a tokamak by magnetic force in order to control the generation of nuclear fusion power [5].

The magnetic field applied to flows in porous domains covers a wide area of application including geothermal energy, metallurgy and nuclear science [6,7]. In the solidification of alloys, a magnetic field is used to adjust the flow pattern in the porous mushy zone [8]. MHD flows of liquid metal in a capillary porous system (CPS) were investigated as a means to obtain better control of head load and surface erosion on the plasma facing components (PFCs) [5,9]. For enhancement of heat transfer, there have been a number of studies which investigated nanofluids subjected to magnetic fields [10–14]. Furthermore, magnetic fields have been applied to blood flows for clinical purposes. Pulsatile flows of blood that were considered electrically conducting through porous media were numerically investigated [15,16].

Thermal behavior of the flow of an electrically conducting fluid through a magnetic field over a stretching sheet embedded in a non-Darcian medium was numerically analyzed, accounting for radiation and heat generation and absorption [17]. The unsteady problem of the laminar fully-developed flow and heat transfer of an electrically-conducting and heat-generating or absorbing fluid with variable properties through a porous channel in the presence of uniform magnetic and electric fields was studied through a parametric study [18]. Later, El-Amin took the combined effects of Ohmic (or Joule) heating and viscous dissipation into consideration to investigate MHD forced convection over a non-isothermal horizontal cylinder in a fluid saturated porous medium [19].

The effects of flow, medium permeability and fractional parameters were analyzed for the flow of eclectically conducting fractional fluid through a porous channel. The exact solution was derived by applying the Caputo–Fabrizo time fractional derivative to find the exact solution. The momentum equation was solved using the joint Laplace and Fourier transform [20].

However, the study of compressibility effects on MHD porous flows has been very limited [21–24]. The influences of magnetic induction and rotation on the thermosolutal instability of a rotating flow in a porous medium was investigated [21]; the fluid was considered compressible, as its fluid density varied with temperature pressure and concentration. Additionally, each temperature pressure and concentration was a function of elevation. The thermal instability of a Rivlin–Ericksen rotating fluid with suspended particles flowing through a porous medium subjected to a magnetic effect was studied [22]; the fluid density varied with both temperature and pressure. In these works [21–24], the representative model for electrically conducting fluid was assumed with constant properties. MHD compressible liquid which flowed through a porous plate was examined [24]; it was found that a differential equation for the density could be linear if gravitational effects were neglected. The recent work on compressible MHD flow through a porous medium has been conducted numerically [25]. In this work, the computed results were nondimensionalized via post processing. Although the overall effect of magnetic-flow interaction on thermal and flow processes was interesting, the Hartman number which represented the magnetic effect was the only parameter examined. Moreover, employing the properties of air in calculations might not reflect the true situation with accuracy.

The present article investigates the unsteady flow and heat transfer of a compressible Helium–Xenon binary gaseous mixture subjected to a magnetic field in a two-dimensional plane. Helium (He)–Xenon (Xe) gaseous mixture is generally adopted as a working fluid in a closed cycle MHD power generation system to avoid using an alkali-metal seed [26,27]. Additionally, the He–Xe mixture is utilized as a coolant in nuclear reactors due to its high heat transfer coefficient [28,29]. The thermal and mechanical properties of the gaseous mixture are considered temperature-dependent. Density of the mixture gas is allowed to change with temperature as well as pressure. The system of dimensionless governing equations is one of the important dimensionless parameters that effectively facilitate parametric analysis. The numerical results are validated using the previously published literature. To our best knowledge, such a study is not found in the existing literature.

## 2. Problem Formulation and Methodology

Figure 1 shows the physical geometry of the problem. A rectangular porous channel with the size of 0.0001 m × 0.0002 m is placed in an x-y coordinate. The binary gaseous mixture of Xe and He with equal component proportion is considered. The gas flows through an inlet section with the mass flow rate given by Equation (1):

$$\rho u_{in} = \rho u_0 \left( \cos \frac{\pi y}{d} \right)^2 \quad (1)$$

where $u_0$ is the peak velocity at the inflow boundary, which will be used as a reference value for the non-dimensionalization process.

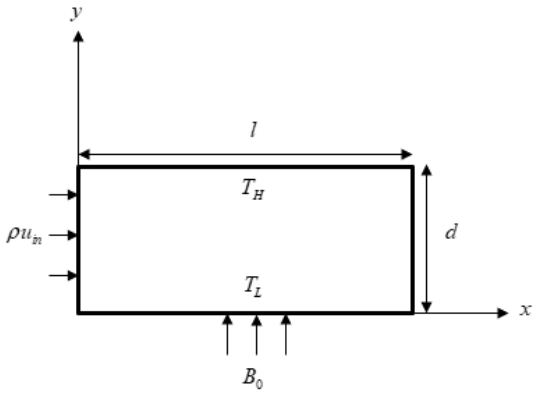


**Figure 1.** Schematic representation of the physical geometry of the problem.

An isothermal condition is imposed on the lateral walls. The top wall has a higher temperature than the bottom wall. The outflow boundary is nonreflecting [30]. The magnetic field propagates from the lower wall to the upper wall across the domain.

### *2.1. Mathematical Model*

The set of governing equations is modeled to describe the non-isothermal flow of electrically conducting fluid through a porous media including mass conservation momentum and energy equations. The Darcy-Brinkman-Forchheimer equation is used to model flow through a porous media [31–33]. In its conservative form, it is written for two-dimensional flow as

$$\frac{\delta}{\delta t}[U] + \frac{\delta}{\delta x}[E_I - E_v] + \frac{\delta}{\delta y}[F_I - F_V] = [H] \tag{2}$$

where $U$, $E$, $F$ and $H$ are column vectors containing flux variables, as follows:

$$[U] = \begin{bmatrix} \rho \\ \rho u \\ \rho v \\ \rho e_t \end{bmatrix} \tag{3}$$

$$[E_I] = \begin{bmatrix} \rho u \\ \rho u^2 + p \\ \rho uv \\ u(\rho e_t + p) \end{bmatrix}; [F_I] = \begin{bmatrix} \rho v \\ \rho uv \\ \rho v^2 + p \\ v(\rho e_t + p) \end{bmatrix} \tag{4}$$

$$[E_V] = \begin{bmatrix} 0 \\ \sigma_{xx} \\ \tau_{xy} \\ -u\sigma_{xx} - v\tau_{xy} - q_x \end{bmatrix}; [F_I] = \begin{bmatrix} 0 \\ \tau_{xy} \\ \sigma_{yy} \\ u\tau_{xy} - v\sigma_{yy} - -q_y \end{bmatrix} \tag{5}$$

$$[H] = \begin{bmatrix} 0 \\ -\frac{u}{K}\left(\mu + \rho\sqrt{u^2 + v^2}\right) - \sigma B_0^2 u \\ -\frac{v}{K}\left(\mu + \rho\sqrt{u^2 + v^2}\right) \\ \sigma B_0^2 u^2 \end{bmatrix} \tag{6}$$

The stress tensor can be expanded in terms of velocity and viscosity, as follows:

$$\sigma_{xx} = -\frac{2}{3}\mu\left(\nabla \cdot \vec{V}\right) + 2\mu\frac{\partial u}{\partial x} \tag{7}$$

$$\sigma_{yy} = -\frac{2}{3}\mu\left(\nabla \cdot \vec{V}\right) + 2\mu\frac{\partial v}{\partial y} \tag{8}$$

$$\tau_{xy} = \mu\left(\frac{\partial u}{\partial y} + \frac{\partial v}{\partial x}\right) \tag{9}$$

The dynamic viscosity and thermal conductivity of the binary gas mixture data are taken from [34] and plotted as a function of temperature in Figure 2.

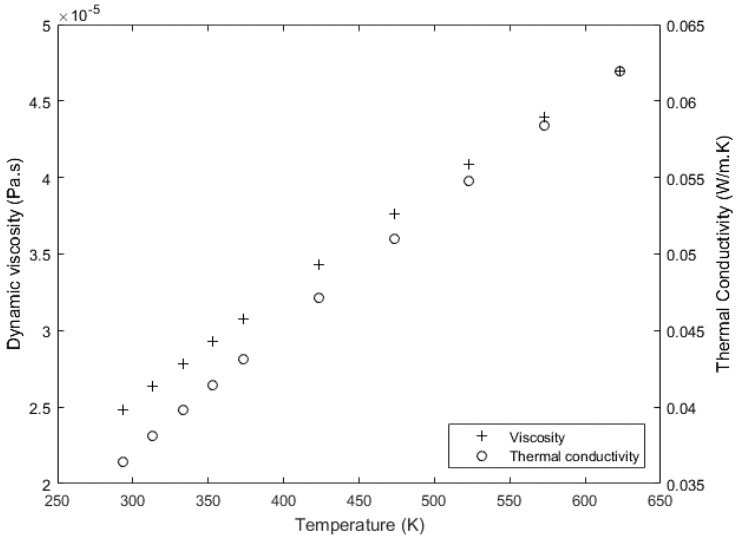


**Figure 2.** Dynamic viscosity and thermal conductivity of the binary gas mixture as a function of temperature.

Subsequently, the temperature dependencies of viscosity ($\mu$) and thermal conductivity ($k$) are modeled using a linear regression approach and given by

$$\mu(T) = 6.72696 \times 10^{-8}T + 5.47652 \times 10^{-6} \tag{10}$$

$$k(T) = 7.75447 \times 10^{-5}T + 1.40533 \times 10^{-2} \tag{11}$$

In a fluid-saturated porous domain, the effective thermal conductivity $k_{eff}$ is considered as

$$k_{eff}(T) = \phi k(T) + (1 - \phi)k_s, \tag{12}$$

where porosity $\phi$ and the Thermal Conductivity of Solid Matrix $k_s$ are taken to be constant at 0.75 and 0.6, respectively.

Considering the compressibility effect, quantities including velocity, temperature, density and pressure, must be satisfied with respect to the total energy and ideal gas law relationships:

$$\rho e_t = \frac{1}{2}\left(\rho u^2 + \rho v^2\right) + \frac{p}{\gamma - 1} \tag{13}$$

$$p = \rho RT \tag{14}$$

### *2.2. Nondimensionalization Process*

The governing equations are rendered non-dimensional using the adopted non-dimensional variables. The existing dimensional variables, which are peak inlet velocity, channel width, initial fluid temperature and density, are used as the reference variables. Definitions of the non-dimensional variables are shown in Table 1.

**Table 1.** Definition of the non-dimensional variables.

| Variable | Definition |
|---|---|
| Length | $\overline{x} = \frac{x}{d}, \overline{y} = \frac{y}{d}$ |
| Velocity | $\overline{u} = \frac{u}{u_{max}}, \overline{v} = \frac{v}{u_{max}}$ |
| Temperature | $\overline{T} = \frac{T}{T_0}$ |
| Total Energy | $\overline{e_t} = \frac{e_t}{u_{max}^2}$ |
| Time | $\overline{t} = \frac{u_{max}}{d}$ |
| Density | $\overline{\rho} = \frac{\rho}{\rho_0}$ |
| Pressure [35] | $\overline{p} = \frac{p}{\rho_0 u_{max}^2}$ |
| Thermal Conductivity | $\overline{k} = \frac{k}{k_0}$ |
| Stress | $\overline{\sigma_x} = \frac{d}{\mu_0 u_0}\sigma_x, \overline{\sigma_y} = \frac{d}{\mu_0 u_0}\sigma_y, \overline{\tau_{xy}} = \frac{d}{\mu_0 u_0}\tau_{xy}$ |

The non-dimensional set of equations with the dimensionless groups derived is:

$$\frac{\delta}{\delta \overline{t}}\left[\overline{U}\right] + \frac{\delta}{\delta \overline{x}}\left[\overline{E_I} - \frac{1}{Re_0}\overline{E_v}\right] + \frac{\delta}{\delta \overline{y}}\left[\overline{F_I} - \frac{1}{Re_0}\overline{F_V}\right] = \left[\overline{H}\right], \tag{15}$$

where

$$\left[\overline{U}\right] = \begin{bmatrix} \overline{\rho} \\ \overline{\rho u} \\ \overline{\rho v} \\ \overline{\rho e_t} \end{bmatrix} \tag{16}$$

$$\left[\overline{E}_I\right] = \begin{bmatrix} \overline{\rho u} \\ \overline{\rho u}^2 + \overline{p} \\ \overline{\rho u v} \\ \overline{u}(\overline{\rho e} + \overline{p}) \end{bmatrix}; \left[\overline{F}_I\right] = \begin{bmatrix} \overline{\rho v} \\ \overline{\rho u v} \\ \overline{\rho v}^2 + \overline{p} \\ \overline{v}(\overline{\rho e} + \overline{p}) \end{bmatrix} \tag{17}$$

$$\left[\overline{E}_V\right] = \begin{bmatrix} 0 \\ \overline{\sigma}_x \\ \overline{\tau}_{xy} \\ \frac{\overline{u}\overline{\sigma}_x + \overline{v}\overline{\tau}_{xy} + \overline{q}_x}{(\gamma-1)Pr_0 \mathrm{Ma}_0^2} \end{bmatrix}; \left[\overline{F}_V\right] = \begin{bmatrix} 0 \\ \overline{\tau}_{yx} \\ \overline{\sigma}_y \\ \frac{\overline{u}\overline{\tau}_{yx} + \overline{v}\overline{\sigma}_y + \overline{q}_y}{(\gamma-1)Pr_0 \mathrm{Ma}_0^2} \end{bmatrix} \tag{18}$$

$$\left[\overline{H}\right] = \begin{bmatrix} 0 \\ -\frac{1}{\mathrm{Gr}_n}\left(\overline{\mu u} + \mathrm{Gr}_f \overline{\rho u}\sqrt{\overline{u}^2 + \overline{v}^2}\right) - N_0 \overline{u} \\ -\frac{1}{\mathrm{Gr}_n}\left(\overline{\mu v} + \mathrm{Gr}_f \overline{\rho v}\sqrt{\overline{u}^2 + \overline{v}^2}\right) \\ N_0 \overline{u}^2 \end{bmatrix} \tag{19}$$

The Dimensionless numbers in the above equations are defined in Table 2.

**Table 2.** Definition of Dimensionless numbers.

| Dimensionless Number | Definition |
|---|---|
| Reynold number | $Re_0 = \frac{\rho_0 u_{max}}{\mu_0}$ |
| Prandtl number | $\mathrm{Pr}_0 = \frac{\mu_0 C p_0}{k_0}$ |
| Hartmann number | $\mathrm{Ha}_0 = B_0 d\sqrt{\frac{\sigma}{\mu_0}}$ |
| Stuart number | $\mathrm{N} = \frac{\mathrm{Ha}_0^2}{Re_0}$ |
| Mach number | $\mathrm{Ma}_0 = \frac{u_{max}}{c_0}$ |
| Coefficient of Inertia [36] | $\mathrm{Gr}_f = \frac{\rho_0 u_{max}\sqrt{K}}{\mu_0}$ |
| Coefficient of Permeability [36] | $\mathrm{Gr}_n = \frac{\rho_0 u_{\max} K}{\mu_0 d}$ |
| Thermal Conductivity | $C_f = \frac{\overline{\mu}\frac{d\overline{u}}{d\overline{y}}}{\frac{1}{2}\overline{\rho} Re_0}$ |
| Nusselt number | $Nu = \frac{d\overline{T}}{d\overline{y}}$ |

The dynamic viscosity and thermal conductivity are

$$\overline{\mu}(\overline{T}) = 7.86552 \times 10^{-1}\overline{T} + 2.13448 \times 10^{-1} \tag{20}$$

$$\overline{k_{eff}}(\overline{T}) = 9.61293 \times 10^{-2}\overline{T} + 8.84514 \times 10^{-1} \tag{21}$$

The equation of state and total energy is

$$\overline{p} = \frac{\overline{\rho}\overline{T}}{\mathrm{Ma}_0^2\gamma} \tag{22}$$

$$\overline{e_t} = \frac{1}{2}\left(\overline{u}^2 + \overline{v}^2\right) + \frac{\overline{p}}{\overline{\rho}(\gamma - 1)} \tag{23}$$

### *2.3. Numerical Procedure and Model Validation*

The compact finite difference scheme is used for spatial discretization [37]. The solution is solved and advanced in time using the 3rd Runge–Kutta method. Each time step is calculated based on the Courrant-Friedrichs-Lewy condition. The CFL value is given to be a constant value that should range between 0.3–0.7 depending on the numerical stability.

The independence test was carried out for the non-isothermal MHD flow. The 49 × 149 resolution was found to be optimal, since the changes in averaged velocity and temperature at the center of the domain were less than 0.5% when finer resolutions were implemented.

The numerical model was validated against previously published work [25]. The focus in the previous study was to investigate the coupled effects of variable properties and magnetic force on thermal and flow processes. The comparative results of the steady state velocities at half of the channel for a varied Hartman number is shown in Figure 3. Excellent agreement is achieved, as the difference between the two results appears minimal.

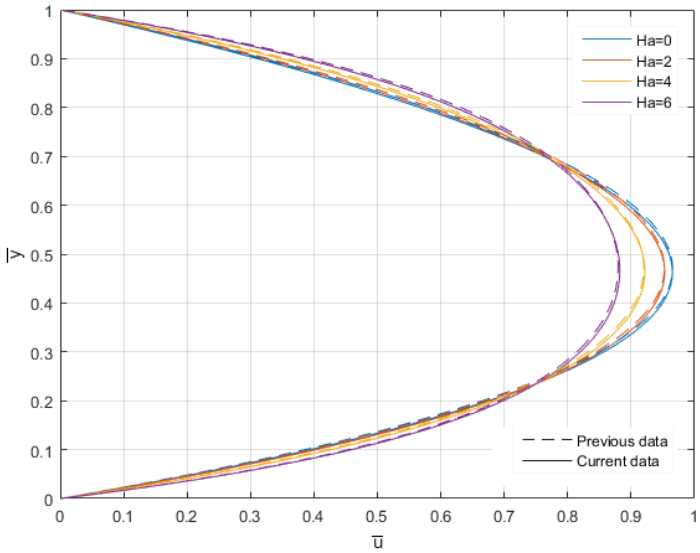


**Figure 3.** Comparison of the predicted steady-state velocity profiles at the midplane channel at different Hartman numbers between the present model and the published work [25].

## 3. Results and Discussion

To investigate the transient effect, the numerical solutions were extracted at four different times for the Reynolds number $Re_0$ = 2300, Prandtl number $Pr_0$ = 0.44, and Mach number $\mathrm{Ma}_0$ = 0.3.

Figure 4 shows a mass flow rate that changes with time for cases both without (N = 0) and with (N = 10) magnetic effect. It is clearly seen that flow through a magnetic field propagates much more slowly than flow without a magnetic field. For the case where

N = 10, fluid motion is retarded by an electromagnetic force, the so-called Lorentz force, exerted on a charge particle.

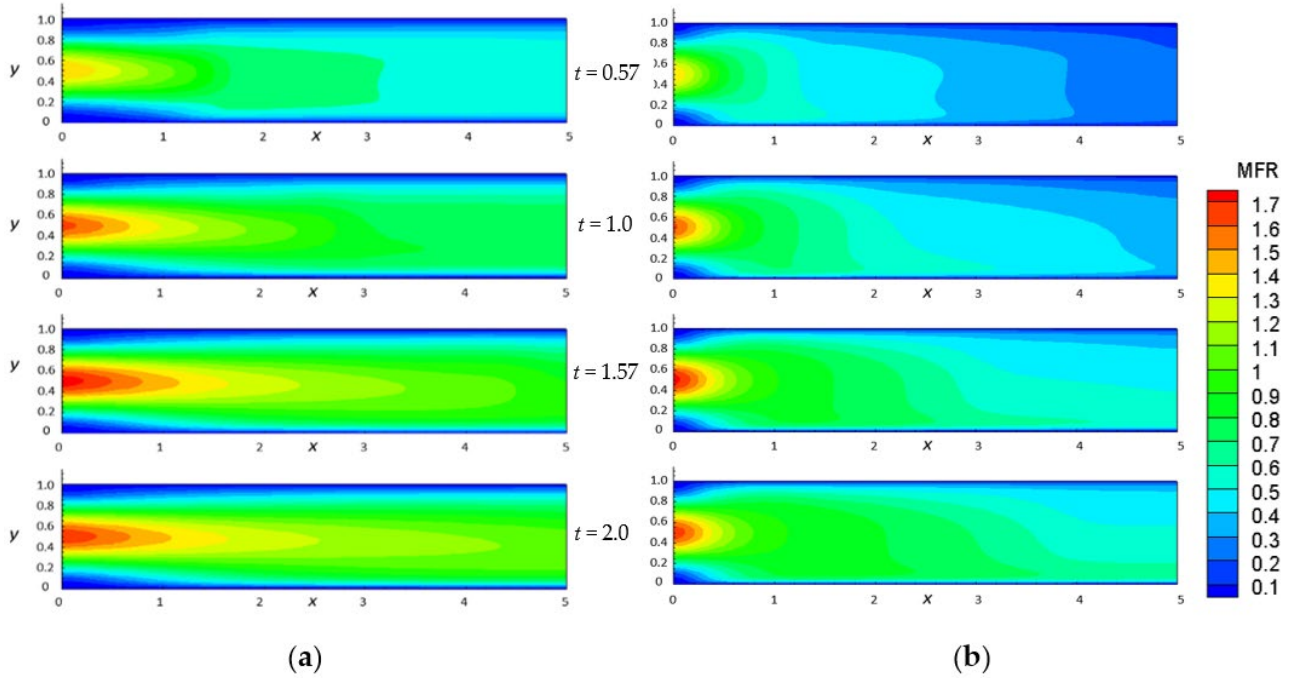


**Figure 4.** Time evolution of mass flow rate at dimensionless times 0.57, 1.0, 1.57 and 2.0 for a Stuart number of (**a**) N = 0 (**b**) N = 10.

Thermal behavior of the two cases was investigated via the time evolution of temperature contours, illustrated in Figure 5. As can be seen, although temperature stratification mainly evolves downward from the upper wall, heat is transported primarily in the flow direction, from the left to the right domain. As evident in Figure 4, the flow is slowed down with a magnetic effect (N = 10), causing a thicker thermal boundary layer.

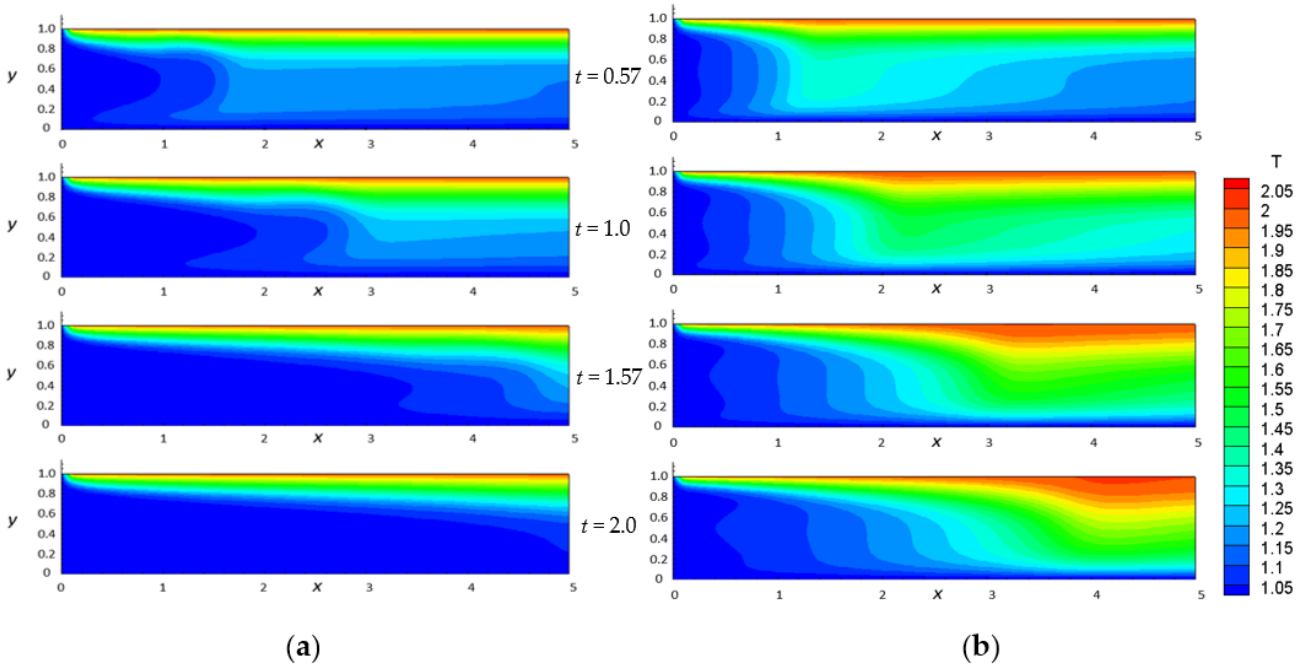


**Figure 5.** Time evolution of field temperature at dimensionless times 0.57, 1.0, 1.57 and 2.0 for a Stuart number of (**a**) N = 0 (**b**) N = 10.

Hereafter, the focus will be on the case of the non-isothermal flow subjected to magnetic force (N = 10). Figure 6 shows the change over time of mass flow rates. The values along the lines crossing at different transverse locations are plotted as well. With respect to the center line of the channel, it is clear that the profile of the flow rate is not symmetric; the non-uniform fluid density causes a mass flow rate greater in the bottom domain than in the upper domain.

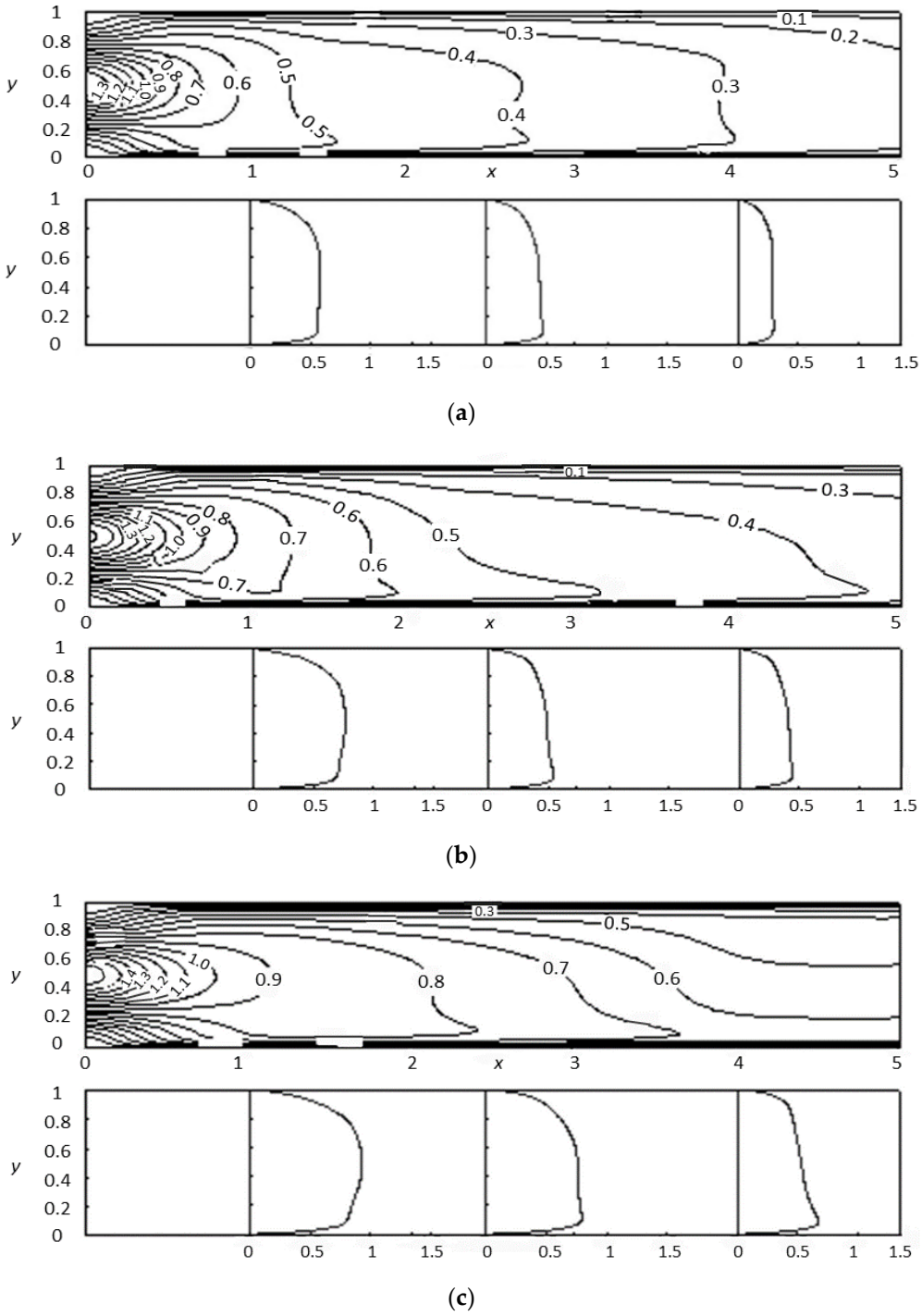


**Figure 6.** Contours of a mass flow rate that progresses at different dimensionless times: (**a**) 0.57; (**b**) 1.0; (**c**) 2.0.

How the fluid density varies can be seen in Figure 7. As seen in this figure, the density is lower towards the top left corner of the domain, where the temperature is high. The

areas where the densities are high correspond to the areas where the mass flow rates are high. This result is consistent with the distribution of mass flow rate shown in Figure 6.

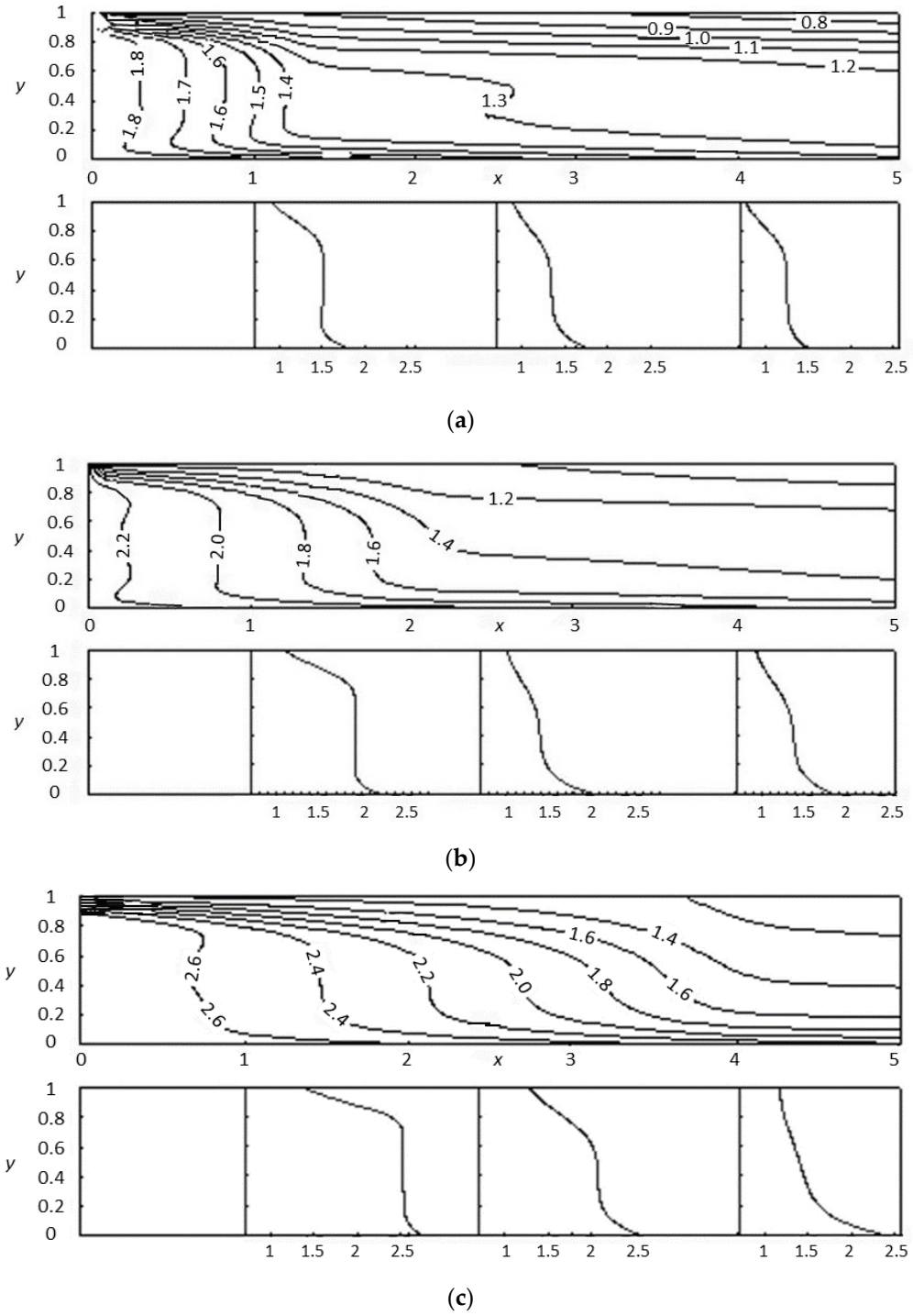


**Figure 7.** Contours of fluid density taken at different dimensionless times: (**a**) 0.57; (**b**) 1.0; (**c**) 2.0.

As briefly mentioned, temperature distributions are depicted throughout the channel in Figure 8. Additionally, temperatures spread more uniformly downstream. With regard to the local wall shear stress relative to dynamic pressure, Figure 9a presents the skin friction coefficient, which changes with the channel distance.

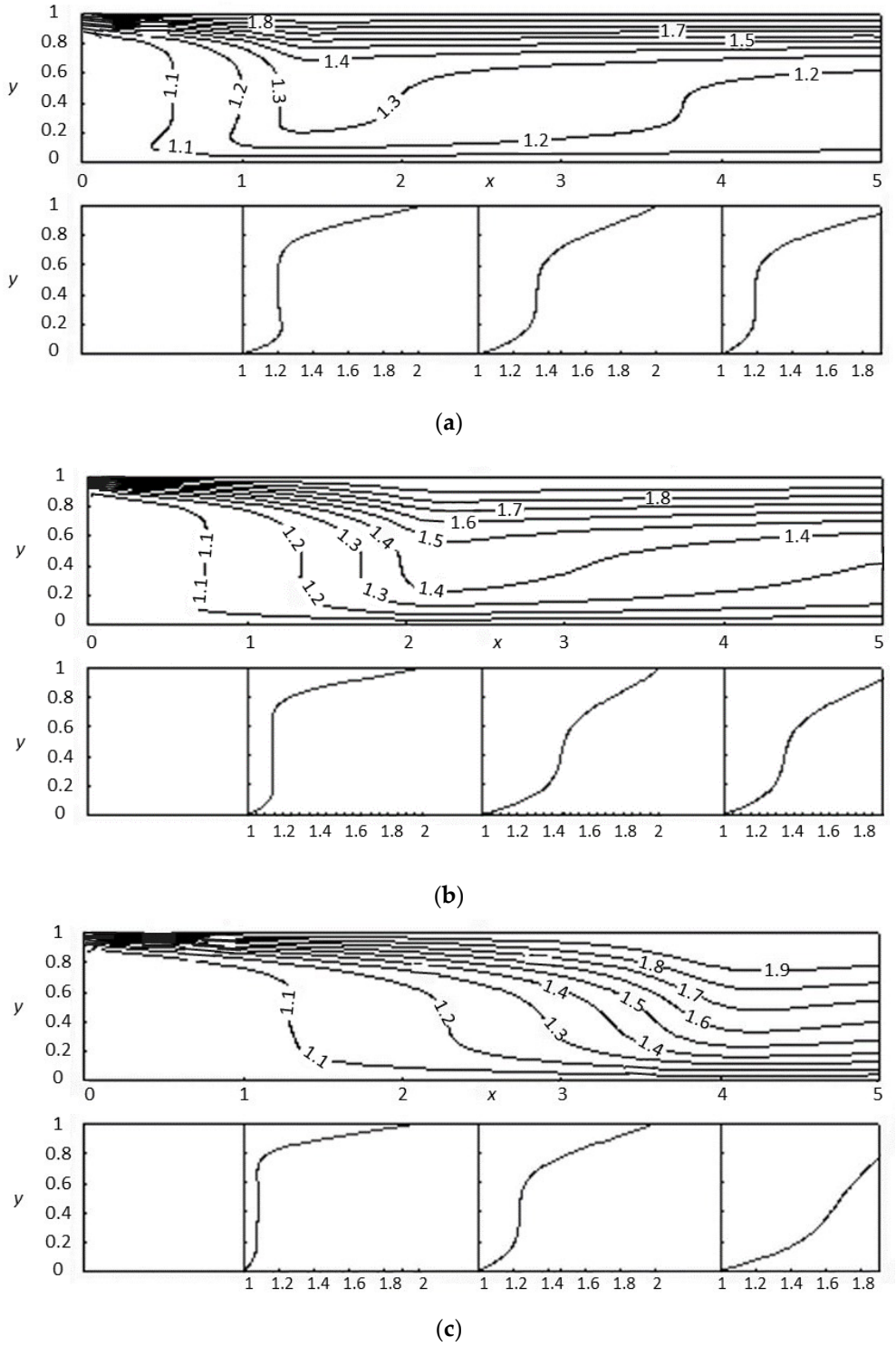


**Figure 8.** Contours of field temperature taken at different dimensionless times: (**a**) 0.57; (**b**) 1.0; (**c**) 2.0.

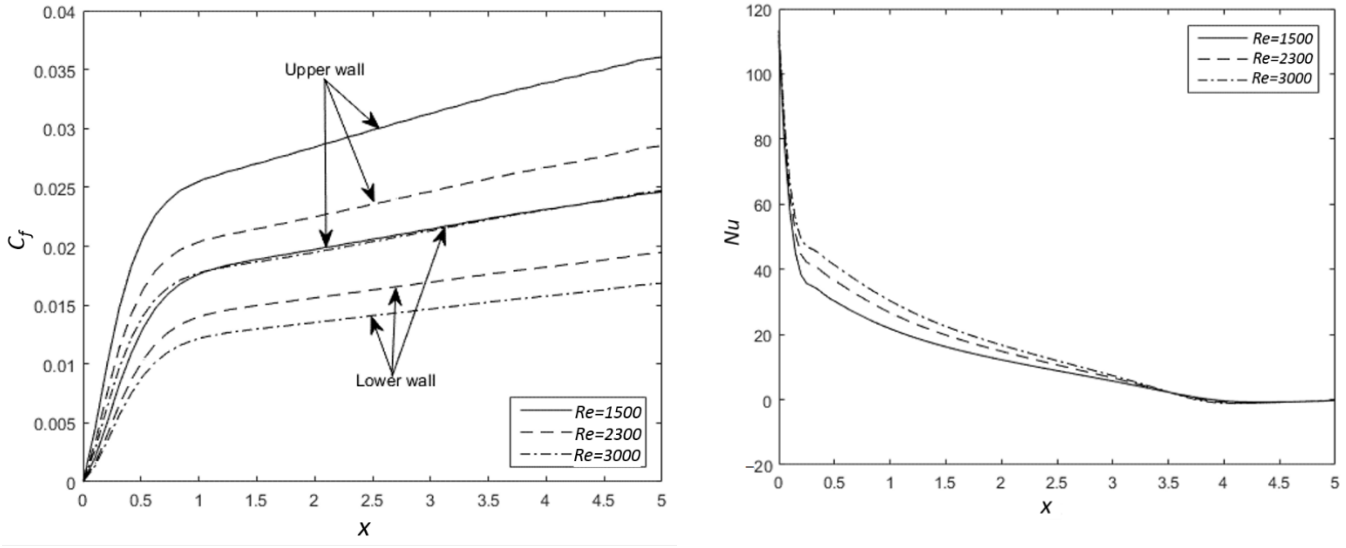


(**a**) (**b**)

**Figure 9.** Wall Skin Coefficient and Nusselt number under different Reynold numbers: (**a**) Skin friction coefficient; (**b**) Nusselt number.

The skin friction coefficient $C_f$ increases significantly as x increases near the channel entrance, owing to the significant increase in the velocity gradient. The $C_f$ value gets larger for a greater Reynolds number as the velocity gradient gets larger, while the boundary layer becomes thinner. Further, the friction coefficient is greater for the upper wall than for the lower wall, indicating a larger velocity gradient at the top wall. This result, which is not axially symmetric, is found to be consistent with the results shown in the previous figures. In order to evaluate the heat transfer enhancement via convected thermal energy, the Nusselt number ($Nu$) is computed and plotted for different $Re_0$ in Figure 9b; it can be seen that the $Nu$ decreases downstream due to the thicker thermal boundary layer. The $Nu$, however, rises with an increased $Re$, since the thermal boundary layer is in turn thinner.

Figure 10a,b illustrates the effects of $Pr$ on $C_f$ and $Nu$, respectively. The friction coefficient $C_f$ is increased with decreased $Pr$ due to a higher ratio of momentum diffusivity to thermal diffusivity. This causes a higher velocity gradient along the walls. However, this effect on $C_f$ can be considered small. On the other hand, Nu is increased with $Pr$ due to the greater inertial force of fluid flow.

The other important parameter considered is the Stuart number, N, which is the influence of magnetic force relative to the inertial force. The respective effects of N on $C_f$ and $Nu$ are given in Figure 11a,b. The friction coefficient is found to vary with N near the channel entrance in the developing region. It is interesting that the trend reverses beginning at around one-fifth of the total channel length as $C_f$ decreases with an increased N. This means that the wall shear stress dominates near the flow entrance for high values of magnetic force, but gets lower farther downstream. In Figure 11b, $Nu$ reveals the same N dependent trend as $C_f$. When N increases, $Nu$ also increases at the entrance region; however, it in turn decreases downstream towards the fully developed region. In this case, heat convection is enhanced with a higher magnetic effect near the entrance, but it is weakened substantially farther towards the channel exit.

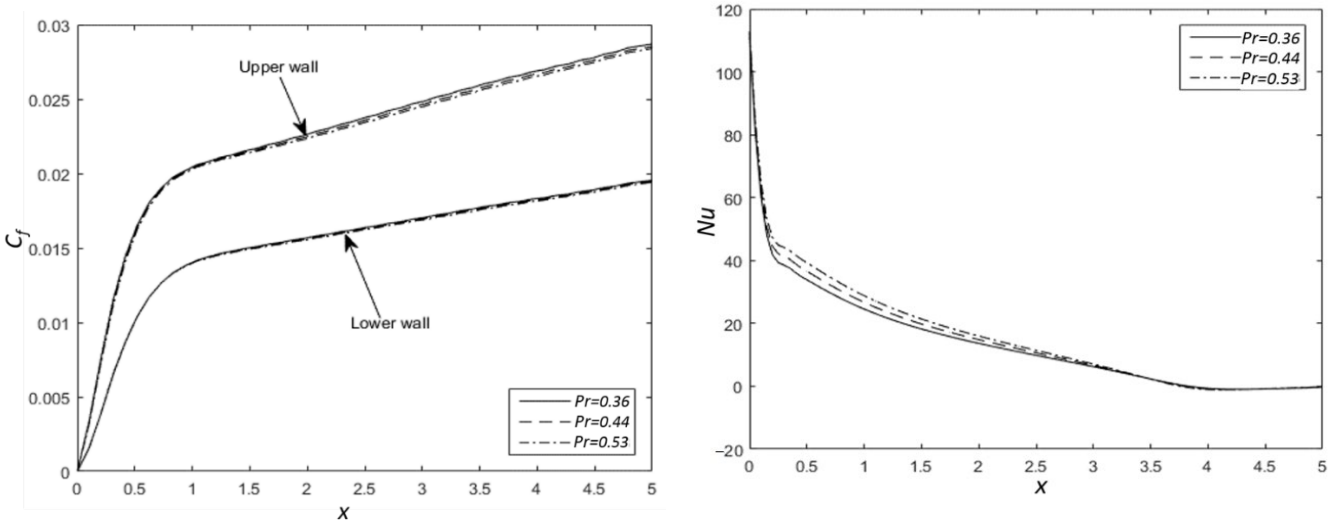


(**a**) (**b**)

**Figure 10.** Wall Skin Coefficient and Nusselt number under different Prandtl numbers: (**a**) Skin friction coefficient; (**b**) Nusselt number.

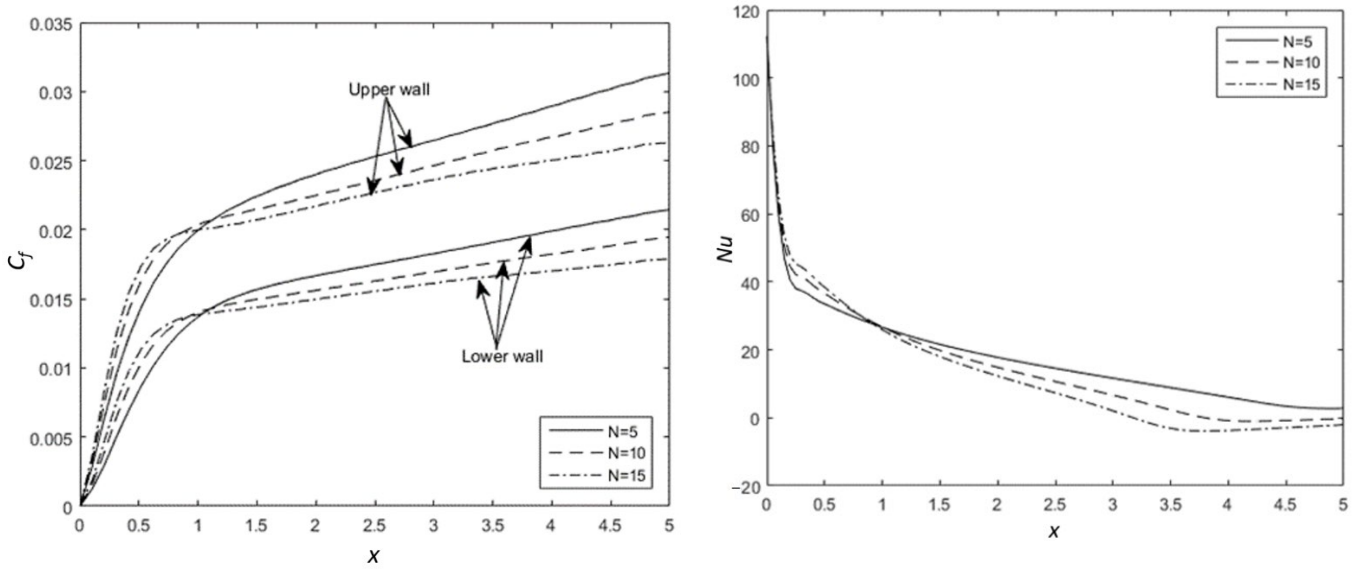


(**a**) (**b**)

**Figure 11.** Wall Skin Coefficient and Nusselt number under different Stuart numbers: (**a**) Skin friction coefficient; (**b**) Nusselt number.

## 4. Conclusions

In this paper, unsteady flow and heat transfer of compressible helium–xenon binary gas through a porous channel subjected to a transverse magnetic field has been numerically investigated. The channel walls are assumed to be non-conducting and maintained at two different temperatures. The electrically conducting binary gas has variable thermal conductivity and viscosity which are the functions of temperature. The effects of magnetic interaction, compressibility and variable fluid properties are examined through parametric dimensionless groups, namely the Reynolds number ($Re_0$), Prandtl number ($Pr_0$) and Stuart number (N). The results show that the magnetic field, compressibility and variable fluid properties considerably affect heat and fluid transport. Variations of density with temperature and pressure result in an asymmetric mass flow profile. Furthermore, the

friction coefficient is greater at the upper wall than at the lower wall due to larger velocity gradients along the top wall. The other findings of this study are as follows:

- The friction coefficient $C_f$ increases for a greater Reynolds number, as the velocity gradient gets larger while the boundary layer becomes thinner. The Nusselt number ($Nu$) rises with an increased $Re_0$, caused a thinner thermal boundary layer.
- The friction coefficient $C_f$ is increased with a decreased Prandtl number $Pr_0$, due to a higher ratio of momentum diffusivity to thermal diffusivity. However, this effect on $C_f$ can be considered small. On the other hand, $Nu$ is increased with $Pr_0$, since the inertial force of fluid flow is larger.
- The friction coefficient $C_f$ is found to vary with the Stuart number N near the channel entrance in the developing region. However, this trend reverses at a certain distance inside the channel, as $C_f$ decreases with an increased N. As N increases, $Nu$ also increases at the entrance region; however, it in turn decreases downstream towards the fully developed region.

**Author Contributions:** Conceptualization, W.P.; Methodology, W.P. and P.P.; Software, W.P.; Investigation, W.P. and P.P.; Writing—original draft preparation, P.P.; Writing—review and editing, W.P.; Supervision, W.P.; Funding acquisition, W.P. All authors have read and agreed to the published version of the manuscript.

**Funding:** This research was funded by Faculty of Engineering, Thammasat University, grant number 009/2563.

**Institutional Review Board Statement:** Not applicable.

**Informed Consent Statement:** Not applicable.

**Data Availability Statement:** Not applicable.

**Acknowledgments:** This work was financially supported by Faculty of Engineering, Thammasat University under Contract No. 009/2563.

**Conflicts of Interest:** The authors declare no conflict of interest.

## References

1. Qian, S.; Bau, H. Magneto-hydrodynamics based microfluidics. *Mech. Res. Commun.* **1998**, *36*, 10–21. [CrossRef]
2. Mishra, S.R.; Dash, G.C.; Acharya, M. Mass and heat transfer effect on MHD flow of a visco-elastic fluid through porous medium with oscillatory suction and heat source. *Int. J. Heat Mass Transf.* **2013**, *57*, 433–438. [CrossRef]
3. Rebhi, R.; Mamou, M.; Hadidi, N. Onset of linear and nonlinear thermosolutal convection with soret and dufour effects in a porous collector under a uniform magnetic field. *Fluids* **2021**, *6*, 243. [CrossRef]
4. Vasu, B.; Gorla, R.S.R.; Murthy, P.V.S.N.; Prasad, V.R.; Bég, O.A.; Siddiqa, S. MHD Free Convection-Radiation Interaction in a Porous Medium—Part I: Numerical Investigation. *Int. J. Appl. Mech. Eng.* **2020**, *25*, 198–218. [CrossRef]
5. Buhler, L.; Mistrangelo, C.; Najuch, T. Magnetohydrodynamic flows in porous structures. *Fusion Eng. Des.* **2015**, *98*, 1239–1243. [CrossRef]
6. Manna, N.K.; Mondal, C.; Biswas, N.; Sarkar, U.K.; Öztop, H.F.; Abu-Hamdeh, N.H. Effect of multibanded magnetic field on convective heat transport in linearly heated porous systems filled with hybrid nanofluid. *Phys. Fluids* **2021**, *33*, 053604. [CrossRef]
7. Geindreau, C.; Auriault, J.L. Magnetohydrodynamic Flows in porous media. *J. Fluid Mech.* **2002**, *466*, 343–363. [CrossRef]
8. Lehmann, P.; Moreau, R.; Camel, D.; Bolcato, R. A simple analysis of the effect of convection on the structure of the mushy zone in the case of horizontal Bridgman solidification. Comparison with experimental results. *J. Cryst. Growth* **1998**, *183*, 690–704. [CrossRef]
9. Evtikhin, V.A.; Vertkov, A.V.; Lyublinski, I.E.; Khripunov, B.I.; Petrov, V.B.; Mirnov, S.V. Research of lithium capillary-pore systems for fusion reactor plasma facing components. *J. Nucl. Mater.* **2002**, *307–311*, 1664–1669. [CrossRef]
10. Nithyadevi, N.; Rajarathinam, M. Effect of inclination angle and magnetic field on convection heat transfer for nanofluid in a porous cavity. *J. Appl. Fluid Mech.* **2016**, *9*, 2347–2358. [CrossRef]
11. Kumari, P.; Nigam, M.; Kumar, S.; Kumar, V.; Raturi, S.; Pargaei, M.; Krishna Murthy, S.V.S.S.; Rathish Kumar, B.V. Magnetic field effect on non-darcy mixed convection from a horizontal plate in a nanofluid-saturated porous medium. *J. Porous Media* **2019**, *22*, 599–610. [CrossRef]
12. Mondal, M.K.; Biswas, N.; Manna, N.K.; Chamkha, A.J. Enhanced magnetohydrodynamic thermal convection in a partially driven cavity packed with a nanofluid-saturated porous medium. *Math. Methods Appl. Sci.* **2021**. Article in Press. [CrossRef]

13. Balla, C.S.; Haritha, C.; Kishan, N.; Rashad, A.M. Magnetohydrodynamic nanofluid flow and heat transfer in a porous cavity containing heated surface. *J. Nanofluids* **2019**, *8*, 577–588. [CrossRef]
14. Ahmed, S.E.; Mansour, M.A.; Rashad, A.M.; Morsy, Z. MHD free convection and sinusoidal heating in a wavy cavity filled with a heat-generating porous medium using Cu–water nanofluids. *Comput. Therm. Sci.* **2020**, *12*, 217–232. [CrossRef]
15. Shah, N.A.; Al-Zubaidi, A.; Saleem, S. Study of Magnetohydrodynamic Pulsatile Blood Flow through an Inclined Porous Cylindrical Tube with Generalized Time-Nonlocal Shear Stress. *Adv. Math. Phys.* **2021**, *2021*, 5546701. [CrossRef]
16. Ponalagusamy, R.; Manchi, R. Mathematical modeling of electro-magnetohydrodynamic pulsatile flow of an elastico-viscous fluid through an inclined porous tapered arterial stenosis. *Math. Eng. Sci. Aerosp.* **2020**, *11*, 237–254.
17. Taklifi, A.; Aghanajafi, C. MHD non-Darcian flow through a non-isothermal vertical surface embedded in a porous medium with radiation. *Meccanica* **2012**, *47*, 929–937. [CrossRef]
18. Chamkha, A.J. Unsteady laminar hydromagnetic flow and heat transfer in porous channels with temperature-dependent properties. *Int. J. Numer. Methods Heat Fluid Flow* **2001**, *11*, 430–448. [CrossRef]
19. El-Amin, M.F. Combined effect of viscous dissipation and Joule heating on MHD forced convection over a non-isothermal horizontal cylinder embedded in a fluid saturated porous medium. *J. Magn. Magn. Mater.* **2003**, *263*, 337–343. [CrossRef]
20. Haq, S.U.; Khan, M.A.; Khan, Z.A.; Ali, F. MHD effects on the channel flow of a fractional viscous fluid through a porous medium: An application of the Caputo-Fabrizio time-fractional derivative. *Chin. J. Phys.* **2020**, *65*, 14–23. [CrossRef]
21. Sunil; Sharma, R.C.; Chan, T. Combined effect of magnetic field and rotation on thermosolutal instability of a compressible fluid in porous medium. *Polym. Plast. Technol. Eng.* **1996**, *35*, 377–391. [CrossRef]
22. Rana, G.C.; Patial, M. Thermal instability of compressible rivlin-ericksen rotating fluid permeated with suspended dust particles in the presence of vertical magnetic field in porous medium. *Int. J. Heat Technol.* **2011**, *29*, 51–55.
23. Islam, M.M.; Tusher Mollah, M.; Hasan, M.S.; Mahmud Alam, M. Numerical solution of unsteady viscous compressible fluid flow along a porous plate with induced magnetic field. *Model. Meas. Control B* **2017**, *86*, 850–863. [CrossRef]
24. Ganesh, S.; Patil, V.S.; Delhi Babu, R.; Chandrasekar, P.; Anish, M. Unsteady magnetohydrodynamic flow of a compressible liquid through a stainless steel plate of porous medium. In Proceedings of the 3rd International Conference on Frontiers in Automobile & Mechanical Engineering, FAME 2020, Chennai, India, 7–9 August 2020.
25. Pakdee, W.; Yuvakanit, B.; Hussein, A.K. Numerical Analysis on the Two-dimensional Unsteady Magnetohydrodynamic Compressible Flow through a Porous Medium. *J. Appl. Fluid Mech.* **2017**, *10*, 1153–1159. [CrossRef]
26. Zhou, B.; Ji, Y.; Sun, J.; Sun, Y. Modified turbulent Prandtl number model for helium–xenon gas mixture with low Prandtl number. *Nucl. Eng. Des.* **2020**, *366*, 110738. [CrossRef]
27. Harada, N.; Le Kien, C.; Tashiro, T. Closed cycle MHD generator using He/Xe working plasma. In Proceedings of the 33rd AIAA Plasmadynamics and Lasers Conference 2020, Maui, HI, USA, 20–23 May 2002.
28. El-Genk, M.S.; Tournier, J.-M. Noble-gas binary mixtures for closed-Brayton-cycle space reactor power systems. *J. Propuls. Power* **2007**, *23*, 863–873. [CrossRef]
29. El-Genk, M.S.; Tournier, J.-M. On the use of noble gases and binary mixtures as reactor coolants and CBC working fluids. *Energy Convers. Manag.* **2008**, *49*, 1882–1891. [CrossRef]
30. Pakdee, W.; Mahalingam, S. Accurate Method to Implement Boundary Conditions for Reacting Flows Based on Characteristic Wave Analysis. *Combust. Theory Model.* **2003**, *7*, 705–712. [CrossRef]
31. Pakdee, W.; Sakkarangkoon, T. Numerical study of an unsteady non-premixed flame in a porous medium based on the thermal equilibrium model. *J. Theor. Appl. Mech.* **2021**, *59*, 401–412. [CrossRef]
32. Vafai, K. *Handbook of Porous Media*; CRC Press: New York, NY, USA, 2005.
33. Marpu, D.R. Forchheimer and Brinkman extended Darcy flow model on natural convection in a vertical cylindrical porous annulus. *Acta Mech.* **1995**, *109*, 41–48. [CrossRef]
34. Kestin, J.; Kniernim, K.; Mason, E.A.; Najafi, B.; Ro, S.T.; Waldman, M. Equilibrium and Transport Properties of the Noble Gases and Their Mixtures at Low Density. *J. Phys. Chem. Ref. Data* **1984**, *13*, 229–303. [CrossRef]
35. Anderson, K.R.; Mahalingam, S.; Hertzberg, J. A Two-Dimensional Planar Computational Investigation of Flame Broadening in Confined Non-Premixed Jets. *Combust. Flame* **1999**, *118*, 233–247. [CrossRef]
36. Cimolin, F.; Discacciati, M. Navier-Stokes/Forchheimer models for filtration through porous media. *Appl. Numer. Math.* **2013**, *72*, 205–224. [CrossRef]
37. Lele, S.K. Compact Finite Difference Schemes with Spectral-like Resolution. *J. Comput. Phys.* **1992**, *103*, 16–42. [CrossRef]